Nano Research 2015, 8(8): 2492–2502
DOI 10.1007/s12274-015-0757-3
Research Article
ISSN 1998-0124
CN 11-5974/O4

Enhanced Li^+ storage properties of few-layered MoS_2–C composite microspheres embedded with Si nanopowder

Seung Ho Choi and Yun Chan Kang (✉)

Department of Materials Science and Engineering, Korea University, Anam-Dong, Seongbuk-Gu, Seoul 136-713, Republic of Korea

Received: 24 November 2014
Revised: 24 February 2015
Accepted: 1 March 2015

KEYWORDS
molybdenum sulfide,
silicon,
anode material,
lithium batteries,
spray pyrolysis

ABSTRACT

A few-layered MoS_2–C composite material is studied as a supporting material for silicon nanopowder. Microspheres of the few-layered MoS_2–C composite embedded with 30 wt.% Si nanopowder are prepared by one-pot spray pyrolysis. The Si nanopowder particles with high capacity are completely surrounded by the few-layered MoS_2–C composite matrix. The discharge capacities of the MoS_2–C composite microspheres with and without 30 wt.% Si nanopowder after 100 cycles are 1,020 and 718 mAh·g^{-1} at a current density of 1,000 mA·g^{-1}, respectively. The spherical morphology of the MoS_2–C composite microspheres embedded with Si nanopowder is preserved even after 100 cycles because of their high structural stability during cycling. The MoS_2–C composite layer prevents the formation of unstable solid–electrolyte interface (SEI) layers on the Si nanopowder. Furthermore, as the MoS_2–C composite matrix exhibits high capacity and excellent cycling performance, these characteristics are also reflected in the MoS_2–C composite microspheres embedded with 30 wt.% Si nanopowder.

1 Introduction

As the technologies for electric vehicles and portable electronic devices develop, Si is considered an extremely promising anode material for lithium-ion batteries (LIBs) with high capacity and fast charging–discharging properties [1–11]. Available abundantly, Si is an outstanding LIB anode material owing to its low discharge potential (< 0.5 V vs. Li/Li^+) and the highest theoretical reversible capacity of approximately 4,200 mAh·g^{-1}, ten times that of commercial graphite anodes (372 mAh·g^{-1}) [1–11]. However, Si experiences a large volume expansion (300%) during the Li^+ insertion–extraction process, resulting in poor cycling properties because of the pulverization of materials and loss of electrical contact between the electronic materials and the current collector [1–11].

Nanostructured materials and C-based composite materials have been developed to control the volume expansion of the Si electrode [12–36]. Various Si-based nanostructured materials, such as hollow nanospheres, cubic nanocrystals, nanowires, and nanotubes, have improved Li^+ storage properties beyond those of bulk materials [12–21]. Although these Si-based nanostructures can tolerate the large change in volume, the formation of an unstable layer at the solid–

Address correspondence to yckang@korea.ac.kr

electrolyte interface (SEI) between the Si surface and the organic electrolyte leads to a low Coulombic efficiency and a decrease in capacity during cycling [8–10, 12, 21]. C-based Si composite materials have attracted attention as promising anode materials with stable and excellent Li^+ storage properties because of their high electrical conductivity and the stress-buffer layer of carbonaceous materials [22–36]. C-based Si composite materials such as Si–graphite, Si–amorphous C, Si–C nanotubes, and Si–graphene have long cycle lives when the Si content in the composite materials is low [22–35]. As the Si content in a Si–C composite increases, the Li^+ storage properties deteriorate. However, high levels of C increase the initial irreversible capacity and decrease the reversible capacity [22–31]. Thus, the search for new replacement C-containing supporting materials for Si anodes remains a great challenge.

In recent years, transition-metal oxides and metal sulfides have been widely studied as anode materials for LIBs for their theoretical capacities, which exceed those of commercial carbonaceous materials [37–43]. Two-dimensional (2D) layered MoS_2 is especially attractive because of its high reversible capacity and good cycling performance. Controlled MoS_2 materials consisting of a single layer or a few layers facilitate a fast Li^+ charging–discharging process, which allows the interlayer distance to relax the strain and lower the barrier for Li^+ intercalation [44–47]. Because the graphene-like layered MoS_2 can be mixed very uniformly with carbonaceous materials, combining the two materials is regarded as a fundamental strategy to enhance the electrochemical properties of a LIB anode. For example, Zhu et al. reported that a single-layered MoS_2–C fiber composite exhibited a high capacity and long cycling stability for LIBs [45]. However, MoS_2-based materials have lower reversible capacities than those of Si-based materials. A layered MoS_2–C composite material with high structural stability during repeated Li^+ insertion and extraction processes could be an efficient supporting material for Si materials with high Li^+ storage capacities. To the best of our knowledge, metal sulfide–Si composite materials have not been studied as anode materials for LIBs applications.

In this study, few-layered MoS_2–C composite microspheres, embedded with Si nanopowder, were prepared by one-pot spray pyrolysis, using ammonium tetrathiomolybdate, polyvinylpyrrolidone (PVP), and Si nanopowder. Few-layered MoS_2 nanosheets embedded in C spheres served as a protective matrix for the Si nanopowder. In addition to accommodating the large volume expansion of the Si nanopowder, the MoS_2–C composite material prevented the formation and propagation of an SEI layer on the Si surface during repeated electrovoltaic cycling. The electrochemical properties of these microspheres were compared with those of microspheres without embedded Si nanopowders.

2 Experimental section

2.1 Synthesis of few-layered MoS_2–C composite microspheres embedded with Si nanopowder

MoS_2–C composite microspheres embedded with Si nanopowder were directly prepared by ultrasonic spray pyrolysis at 800 °C; a schematic of the apparatus is shown in Fig. S1 (in the Electronic Supplementary Material (ESM)). A quartz reactor measuring 1,200 mm in length and 50 mm in diameter was used; the nitrogen (carrier gas) flow rate was 10 $L \cdot min^{-1}$. The spray solution was formed from 500 mL distilled water, 1.8 g ammonium tetrathiomolybdate, and 5.0 g PVP. Si nanopowder with average particle diameter of 85 nm was dispersed in the spray solution with the ammonium tetrathiomolybdate and PVP.

2.2 Characterization

The crystal structure of the MoS_2–C composite microspheres embedded with Si nanopowder was investigated by X-ray diffractometry (XRD; X'pert PRO MPD, PANalytical, the Netherlands), using Cu Kα radiation (λ = 1.5418 Å). The morphological features were investigated using field-emission scanning electron microscopy (FE-SEM; S-4800, Hitachi, Japan) and high-resolution transmission electron microscopy (HR-TEM; JEM-2100F, JEOL, Japan) at a working voltage of 200 kV. The specific surface areas of the composite microspheres were calculated from a Brunauer–Emmett–Teller (BET) analysis of nitrogen adsorption isotherms (TriStar 3000 gas adsorption analyzer, Micromeritics, USA). The composite microspheres were also investigated using

X-ray photoelectron spectroscopy (XPS; ESCALAB 210, VG Scientific, now Thermo Scientific, USA) with Al Kα radiation (1,486.6 eV).

2.3 Electrochemical measurements

The capacities and cycling properties of the composite microspheres were determined using a 2032-type coin cell. The electrode was prepared from a mixture containing 70 wt.% of the active material, 15 wt.% of Super P (conductive carbon black), and 15 wt.% of sodium carboxymethyl cellulose (CMC) as the binder. Li metal and a microporous polypropylene film were used as the counter electrode and separator, respectively. The electrolyte was 1 M $LiPF_6$ in a 1:1 (v/v) mixture of ethylene carbonate and dimethyl carbonate (EC–DMC) with 5% fluoroethylene carbonate. The charge–discharge characteristics of the samples were determined through cycling in the potential range of 0.001–3.0 V at various fixed current densities. The cyclic voltammetry (CV) measurements were carried out at a scan rate of 0.1 $mV \cdot s^{-1}$. The dimensions of the negative electrode were 1 cm × 1 cm and the mass loading was approximately 1.2 $mg \cdot cm^{-2}$.

3 Results and discussion

Scheme 1 shows the formation mechanism of the few-layered MoS_2–C composite microspheres embedded with Si nanopowder via the one-step continuous spray-pyrolysis process. Droplets are formed from the colloidal spray solution, consisting of Si nanopowder dispersed in an aqueous solution of ammonium tetrathiomolybdate and PVP. In this process, PVP acts as both a stabilizer for the Si nanopowder and the source material for amorphous carbon, thus preventing the stacking of MoS_2 layers [45, 48]. In the precursor solution, the surface of the Si nanopowder is functionalized with water-soluble PVP. The drying of each droplet produces a composite microsphere of Si–ammonium tetrathiomolybdate–PVP in the front part of the reactor, maintained at 800 °C. Thermal decomposition of ammonium tetrathiomolybdate into MoS_2 and carbonization of PVP under the nitrogen atmosphere results in a Si–MoS_2–C composite microsphere at the rear part of the reactor. In other words, one MoS_2–C composite microsphere embedded with Si nanopowder is formed by the drying and decomposition of one droplet, with few-layered

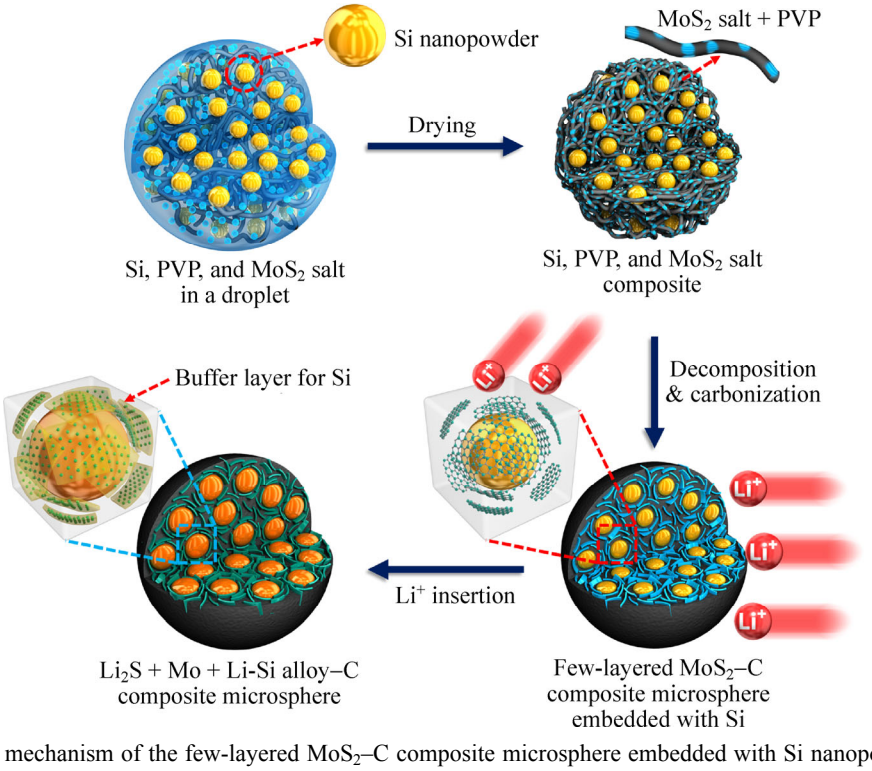

Scheme 1 Formation mechanism of the few-layered MoS_2–C composite microsphere embedded with Si nanopowder via the one-step and continuous spray-pyrolysis process.

ultra-small nanoplates of MoS_2 embedded within the MoS_2–C composite microsphere. The MoS_2–C composite layers, with their elastic two-dimensional structure, completely cover the individual Si nanopowder particles. The Si content in the composite microsphere could be controlled by changing the amount of Si nanopowder dispersed in the spray solution.

The morphologies of the MoS_2–C composite microspheres containing a small amount of enclosed Si nanopowder are shown in Fig. 1. The designed Si content in the composite microspheres shown in Fig. 1 is 30 wt.% based on MoS_2. The morphology of the commercial Si nanopowder used in this study is shown in Fig. S2 (in the ESM); the nanopowder has a mean particle size of 85 nm and a slightly aggregated structure. The FE-SEM and low resolution TEM images reveal the spherical shape of the composite microspheres and the lack of tendency to aggregate. The surface of the composite powder, as shown in Fig. 1, has an embossed structure owing to the Si nanopowder enclosed within the composite microsphere. TEM images (Figs. 1(d) and 1(e)) show the Si nanopowder dispersed within the MoS_2–C matrix. Figures 1(e) and 1(f) show the amorphous-fluid-like structure of the MoS_2–C matrix, in which few-layered MoS_2 nanosheets are uniformly distributed within the amorphous C matrix; the Si nanopowder, which forms an embossed structure, is fully covered by MoS_2–C layers, as shown by the arrows. The enlarged TEM image in the inset of Fig. 1(f) reveals clear lattice fringes separated by a distance of 0.31 nm, corresponding to the interplanar distance of the (111) planes of a Si nanoparticle [19]. The elemental mapping images in Fig. 1(g) show the distributions of MoS_2, C, and Si nanopowder. The necking between the Si nanopowder particles results in some segregation of the Si component in the low-resolution elemental mapping images, as shown in Fig. S3 (in the ESM). MoS_2 and C are uniformly distributed all over the composite microspheres. The Si nanopowder was also well-dispersed within the MoS_2–C composite matrix. Dozens of Si nanopowder particles are dispersed in one composite microsphere, as shown in Fig. 1(g). Considering that MoS_2 converts to MoO_3 when heated

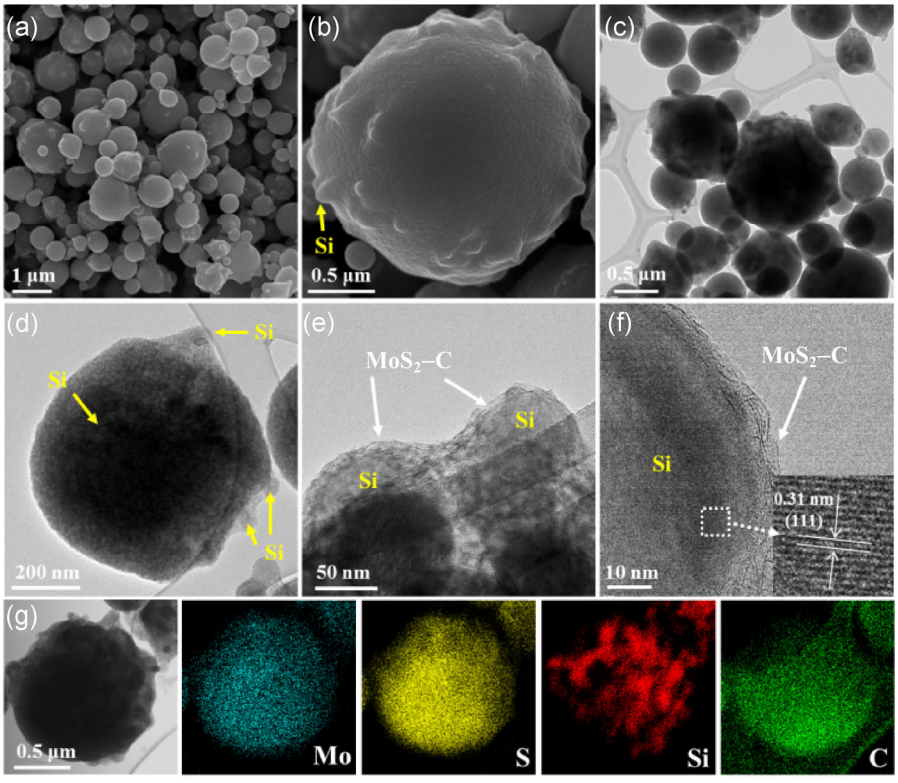

Figure 1 Morphologies of the MoS_2–C composite microspheres embedded with 30 wt.% Si nanopowder. (a) and (b) FE-SEM images, (c)–(f) TEM images, (g) elemental mapping images of Mo, S, Si, and C components.

in air, the C content in the composite microspheres is estimated to be 23 wt.%, as measured by thermogravimetric analysis (see Fig. S4 in the ESM).

The morphologies of the MoS_2–C composite microspheres embedded with a high amount of Si nanopowder are shown in Fig. 2. The designed Si content in the composite microspheres is 60 wt.% based on MoS_2. The composite microsphere shown in Fig. 2 has a more embossed structure than the microspheres shown in Fig. 1 because of the higher Si nanopowder content. The Si nanopowder is well dispersed within the composite microspheres, as shown by the arrows in Figs. 2(d) and 2(e). The Si nanopowder located near the surface of the composite microsphere, as shown in Fig. 2(f), have a uniform MoS_2–C composite coating. The elemental mapping images in Fig. 2(g) also show uniform distributions of MoS_2, C, and Si nanopowder within the composite microsphere. The morphologies of the MoS_2–C composite microspheres are shown in Fig. S5 (in the ESM). The composite microspheres have completely spherical shapes and show no tendency to aggregate. The HR-TEM image in Fig. S5(d) (in the ESM) shows the uniform distribution of MoS_2 nanosheets over the entire C matrix formed from the carbonization process that restricted the number of MoS_2 layers.

The structural characteristics of the MoS_2–C composite microspheres embedded with Si nanopowder are shown in Fig. 3. The XRD patterns of the composite microspheres with low and high amounts of Si nanopowder have broad peaks corresponding to a hexagonal MoS_2 structure and sharp peaks indicating the Si phase. Broad peaks from MoS_2 layers are observed at 2θ values of approximately 33° and 59°. However, the (002) reflections of stacked MoS_2 layers at $2\theta \approx 16°$ are not observed, indicating the presence of only few-layered MoS_2 [45–47]. Therefore, the results of the XRD patterns confirm the formation of few-layered MoS_2 nanosheets in the MoS_2–C composite microspheres embedded with Si nanopowder. Figures 3(b)–3(d) shows the XPS peaks of the MoS_2–C composite microspheres embedded with 30 wt.% Si nanopowder. The C1s XPS peak centered at 284.6 eV in Fig. 3(b), which corresponds to the binding energy of the sp^2 C–C bond, confirms the formation of amorphous C by the carbonization process of PVP

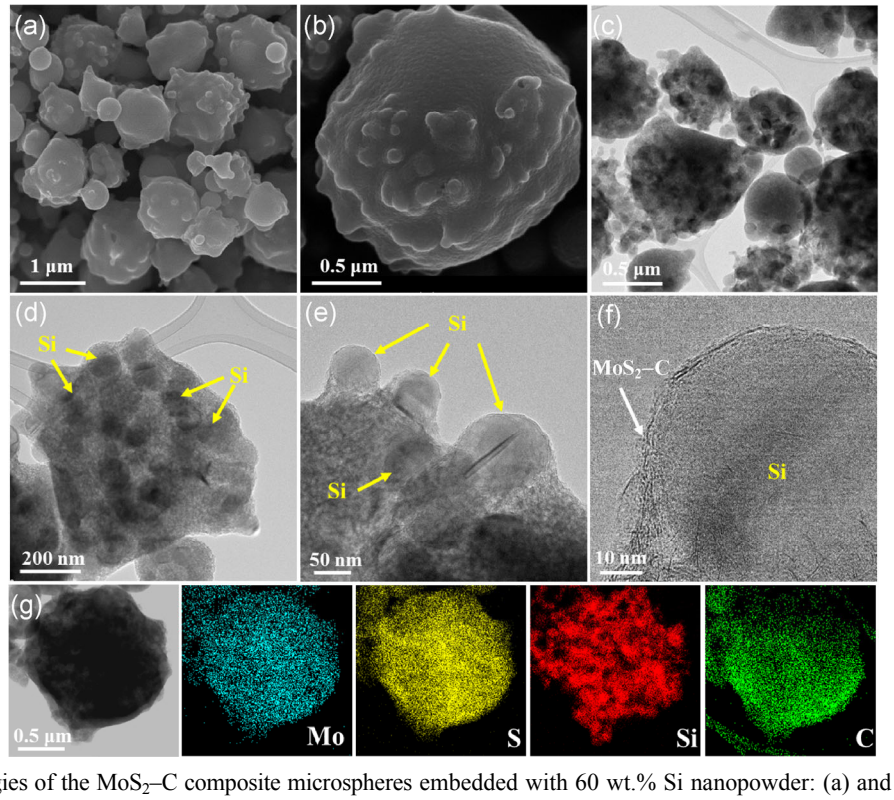

Figure 2 Morphologies of the MoS_2–C composite microspheres embedded with 60 wt.% Si nanopowder: (a) and (b) FE-SEM images, (c)–(f) TEM images, and (g) elemental mapping images of Mo, S, Si, and C components.

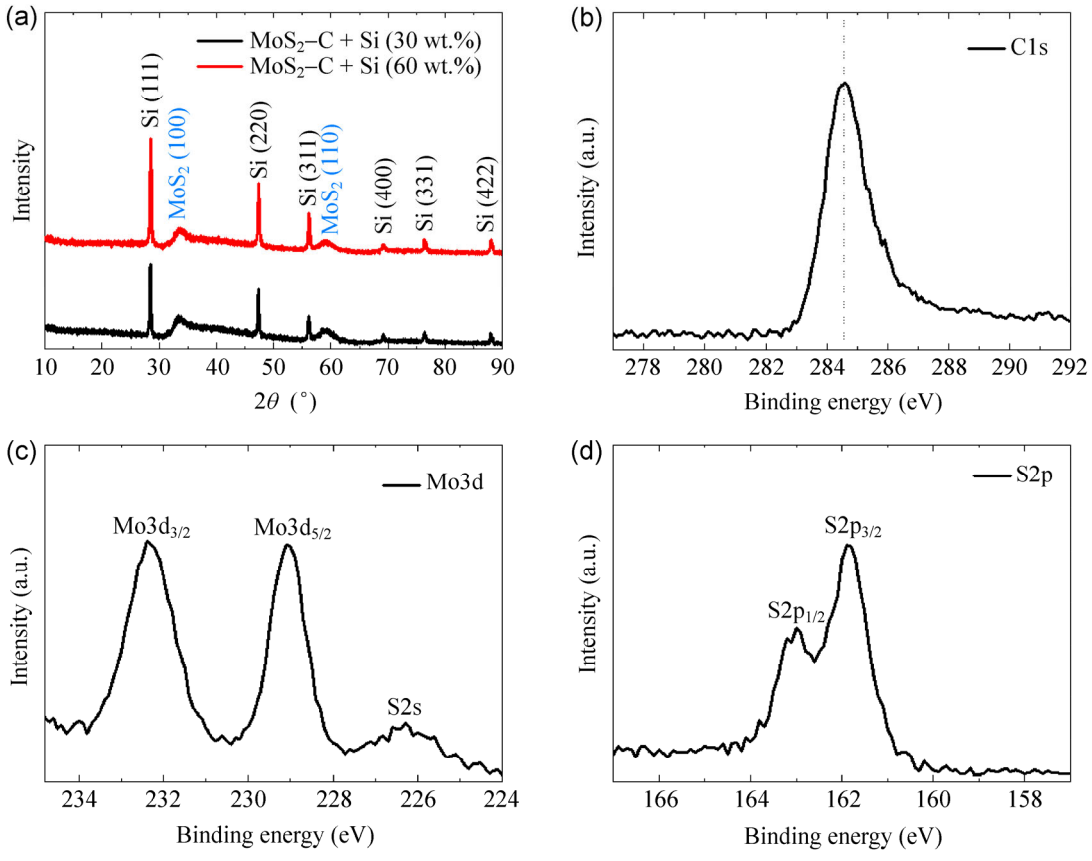

Figure 3 Properties of the MoS_2–C composite microspheres embedded with 30 wt.% and 60 wt.% Si nanopowder. (a) XRD patterns, (b) XPS C1s spectrum of the MoS_2–C composite microspheres embedded with 30 wt.%, (c) XPS Mo3d spectrum, (d) XPS S2p spectrum.

[49]. Two strong Mo3d XPS peaks at around 229.4 and 232.5 eV in Fig. 3(c), which can be attributed to the $Mo3d_{5/2}$ and $Mo3d_{3/2}$ binding energies of MoS_2, respectively, confirm the formation of MoS_2 by the decomposition of ammonium tetrathiomolybdate [50, 51]. The peaks at 162.0 and 163.1 eV, also shown in Fig. 2(d), can be indexed to S2p [50, 51]. The negligible peak intensities of Si2p in Fig. S6 (in the ESM) confirm that the Si nanopowder particles are completed covered by MoS_2–C composite layers. The BET surface areas of the MoS_2–C composite microspheres with 0 and 30 wt.% Si nanopowder were 17.0 and 64.3 $m^2 \cdot g^{-1}$, respectively. The addition of Si nanopowder increases the porosity of the MoS_2–C composite microspheres, as shown in Fig. S7 (in the ESM).

The electrochemical properties of the MoS_2–C composite microspheres with and without embedded Si nanopowder are presented in Fig. 4. Figure 4(a) shows the cyclic voltammogram curves of the composite microspheres with 30 wt.% Si during the first four cycles at a scan rate of 0.1 $mV \cdot s^{-1}$ in the voltage range of 0.001–3 V. Three reduction peaks resulting from Li^+ insertion into MoS_2 and Si were observed in the first cathodic scan. The first reduction peak located at 1.4 V is attributed to the intercalation of Li^+ into the hexagonal MoS_2 lattice, followed by the phase transformation to octahedral Li_xMoS_2 [44–47, 52–56]. The peak at around 0.6 V corresponds to the conversion reaction, in which Li_xMoS_2 decomposes into metallic Mo nanocrystals embedded in a Li_2S matrix, and the formation of a SEI layer on the MoS_2–C surface, resulting from electrochemically driven electrolyte degradation [44–47, 52–54]. The third reduction peak located at 0.05 V is attributed to the reaction forming Li–Si alloys [12–21]. In the first anodic scan, three oxidation peaks attributed to metallic Mo nanocrystals and Li–Si alloys were observed. The first two anodic peaks observed at voltages of 0.3 and 0.55 V are attributed to the de-alloying reactions of Li–Si alloys

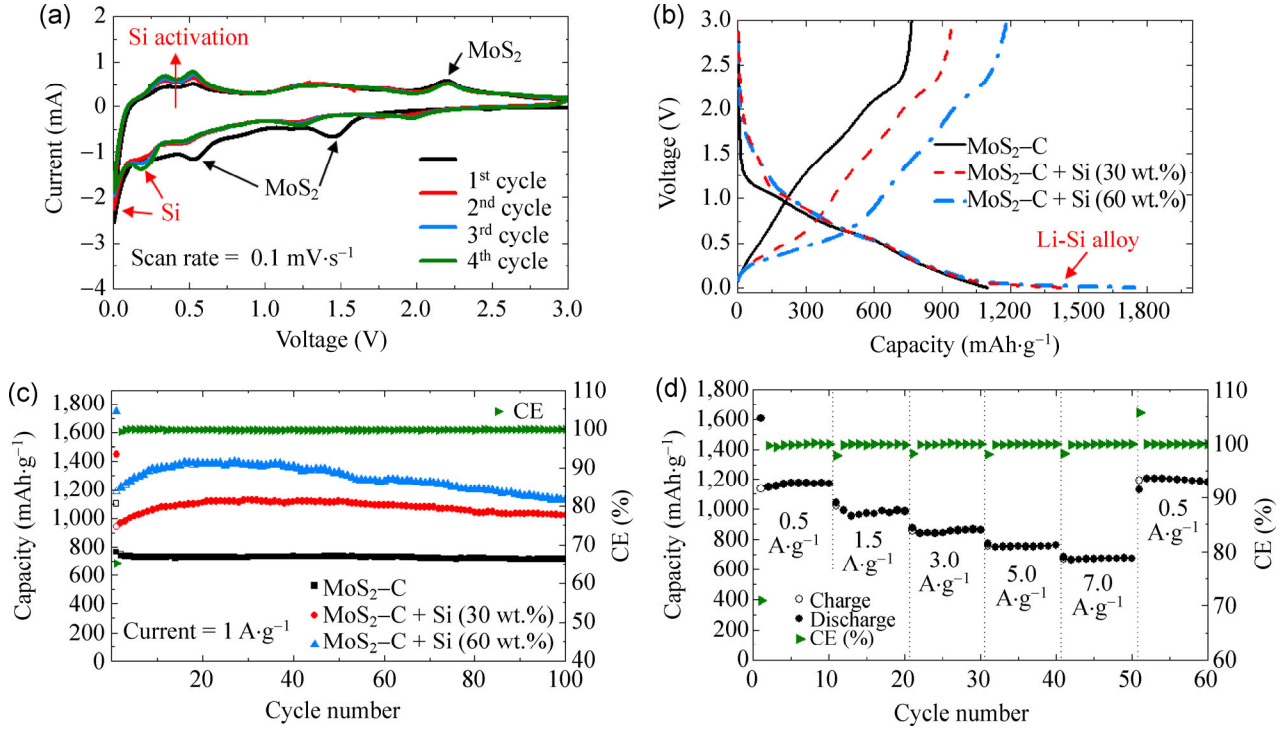

Figure 4 Electrochemical properties of the MoS_2–C without Si nanopowders and MoS_2–C composite microspheres embedded with 30 wt.% and 60 wt.% Si nanopowders: (a) CV curves of MoS_2–C composite microspheres embedded with 30 wt.% Si, (b) initial charge/discharge curves at a current density of 1 $A \cdot g^{-1}$, (c) cycling performances at a current density of 1 $A \cdot g^{-1}$, (d) high rate performances.

[12–21]. The third anodic peak is observed at a voltage of 2.3 V, corresponding to the conversion reaction of metallic Mo and Li_2S to MoS_2 [52–56]. From the second cycle onward, the reduction and oxidation peaks overlap considerably, indicating the excellent reversible cycling performance of the MoS_2–C composite microspheres with 30 wt.% Si. Figure 4(b) shows the initial discharge and charge curves of the MoS_2–C composite microspheres both with and without embedded Si nanopowder, at a current density of 1,000 $mA \cdot g^{-1}$. The initial discharge curves of the composite microspheres with embedded Si nanopowder have clear plateaus at around 0.1 V, owing to the alloying reaction between Li and Si. However, the obvious plateaus corresponding to the formation of Li_xMoS_2 and Mo nanocrystals embedded in a Li_2S matrix are not observed in the initial discharge curves of the three samples, due to the amorphous-fluid-like structure of the MoS_2–C composite. The initial discharge capacities of the MoS_2–C composite microspheres with 0, 30 wt.%, and 60 wt.% Si nanopowder are 1,100, 1,448, and 1,746 $mAh \cdot g^{-1}$, respectively, and their initial Coulombic efficiencies are 69.5%, 65.3%, and 67.8%, respectively.

The cycling performances of the three samples at a current density of 1,000 $mA \cdot g^{-1}$ are shown in Fig. 4(c). The MoS_2–C composite microspheres without Si nanopowder have discharge capacities of 740 and 718 $mAh \cdot g^{-1}$ for the 2nd and 100th cycles, respectively. The capacity retention of the MoS_2–C composite microspheres without Si nanopowder, measured from the 2nd cycle, is 97%, indicating that the few-layered MoS_2–C composite microspheres have excellent cycling performance even at a high current density of 1,000 $mA \cdot g^{-1}$. The discharge capacities of the MoS_2–C composite microspheres with embedded Si nanopowder increase during cycling for the first 20 cycles. The gradual activation of the highly crystalline Si nanopowder during the first 20 cycles increases the capacities of the composite microspheres with increasing cycle number [28, 57]. The increase in the oxidation peak intensity in the CV curves in Fig. 3(a), related to the de-alloying of Li–Si during cycling, also indicates the gradual activation of the Si nanopowder. After achieving its maximum value of 1,390 $mAh \cdot g^{-1}$, the

discharge capacity of the composite microspheres with 60 wt.% Si nanopowder decreases steadily to 1,129 mAh·g^{-1} at the 100th cycle. However, the composite microspheres with 30 wt.% Si nanopowder show stable discharge capacities during further cycling after achieving their maximum capacity at the 20th cycle, and have a capacity of 1,020 mAh·g^{-1} at the 100th cycle. The embedded Si nanopowder increases the capacities of the MoS_2–C composite microspheres. The Coulombic efficiencies of the composite microspheres embedded with 30 wt.% Si nanopowder (Fig. 4(c)) have values above 99.5% from the 2nd cycle. The Li^+ storage properties of these MoS_2–C composite microspheres were compared with those of MoS_2 powders prepared by the spray pyrolysis process reported in the previous literature [52]. The bare MoS_2 powders with filled and yolk-shell structures had discharge capacities of 362 and 687 mAh·g^{-1} for the 100th cycle, respectively, at a current density of 1 A·g^{-1}. This confirms that the embedding of high-capacity Si nanopowder improved the Li^+ storage properties of the MoS_2 material.

Electrochemical impedance spectroscopy (EIS) was conducted to confirm the superior electrochemical properties of the MoS_2–C composite microspheres embedded with 30 wt.% Si nanopowder. The impedance measurements were carried out at room temperature before and after 10, 30, 50, and 100 cycles, at a current density of 1,000 mA·g^{-1}. The resulting Nyquist plots, shown in Fig. S8 (in the ESM), depict a semicircle in the medium-frequency range, which is assigned to the charge-transfer resistance of the electrodes, and a line inclined at approximately 45° to the real axis at low frequencies, corresponding to Li diffusion within the electrode [58, 59]. The charge-transfer resistance of the electrode decreases after the first cycle, owing to the transformation of its crystalline structure into an amorphous-fluid-like structure during the first discharge process. The charge-transfer resistance then remains constant through the 100th cycle. The line inclined at 45° to the real axis at low frequencies is also well-maintained during the first 100 cycles, indicating the good Li^+-diffusion properties of the electrode. The morphology of the composite microspheres embedded with 30 wt.% Si nanopowder after 100 cycles are shown in Fig. S9 (in the ESM). The spherical shape of the composite microspheres remains even after 100 cycles because of their high structural stability during cycling, as the high-capacity Si nanopowder is completely surrounded by the few-layered MoS_2–C composite matrix. The elemental mapping images reveal uniform distributions of MoS_2, C, and Si nanopowder within the composite microsphere, even after cycling. The elastic MoS_2–C composite matrix accommodated the large volume change of the Si nanopowder during repeated Li^+ insertion–extraction. As a result, the formation of a stable SEI layer outside the surface during cycling improved the electrochemical properties of the composite microspheres, while the MoS_2–C composite layer prevented the formation of unstable SEI layers on the Si nanopowder itself. Furthermore, the MoS_2–C composite matrix exhibited high capacities and excellent cycling performances, which then contributed to the capacity and performance of the composite microspheres embedded with 30 wt.% Si nanopowder. The rate performance of the MoS_2–C composite microspheres embedded with 30 wt.% Si nanopowder is shown in Fig. 4(d). The current density increases stepwise from 0.5 to 7 A·g^{-1}; for each step, 10 cycles are measured to evaluate the rate performance. The stable reversible discharge capacities of the composite microspheres decreases from 1,175 to 677 mAh·g^{-1} as the current density increases from 0.5 to 7 A·g^{-1}. The discharge capacity of the composite microspheres recovers to 1,190 mAh·g^{-1} as the current density is reduced to 0.5 A·g^{-1}.

Figure 5 shows the long-term cycling performance of the MoS_2–C composite microspheres embedded with 30 wt.% Si nanopowder at an extremely high current density of 5 A·g^{-1}. The gradual activation during

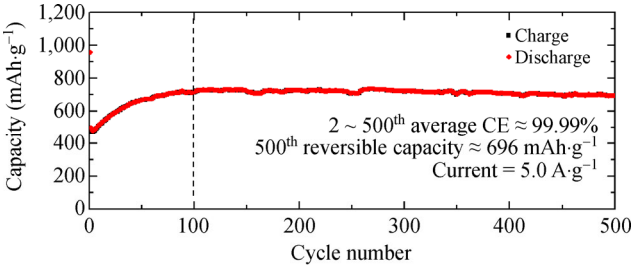

Figure 5 Long-term cycling properties of the MoS_2–C composite microspheres embedded with 30 wt.% Si at a current density of 5.0 A·g^{-1}.

cycling for the first 100 cycles increases the discharge capacities of the composite microspheres. The composite microspheres attain their maximum discharge capacity of 728 $mAh \cdot g^{-1}$ after the first 100 cycles and then steadily maintain this capacity for another 400 cycles. The discharge capacity of the composite microspheres for the 500th cycle is 696 $mAh \cdot g^{-1}$; their capacity retention, measured from the 100th cycle, is 95.4%.

4 Conclusions

A few-layered MoS_2–C composite with high charge and discharge capacities and good cycling performance was successfully applied as a protective matrix for Si nanopowder as an anode material in LIBs. Each MoS_2–C composite microsphere embedded with Si nanopowder was formed by drying and decomposing one droplet containing ammonium tetrathiomolybdate, PVP, and Si nanopowder. The MoS_2–C composite material accommodated the large volume expansion of the Si nanopowder, and also prevented the formation and propagation of a damaging SEI layer on the Si surface during repeated cycling. The embedded Si nanopowder increased the capacity of the MoS_2–C composite microspheres, and its volume fraction in the composite microspheres could be controlled by changing the amount of Si nanopowder dispersed in the spray solution. The amount of MoS_2 and carbon in the composite microspheres could also be controlled by changing the concentrations of ammonium tetrathiomolybdate and PVP dissolved in the spray solution. The composite microspheres of MoS_2, C, and Si with enhanced Li^+ storage properties were evaluated to be a novel anode material with superior electrochemical properties for LIBs.

Acknowledgements

This work was supported by the National Research Foundation of Republic of Korea (NRF) grant funded by the Republic of Korea government (MEST) (No. 2012R1A2A2A02046367). This work was supported by the Creative Industrial Technology Development Program (No. 10045141) funded By the Ministry of Trade, industry & Energy (MI, Republic of Korea).

Electronic Supplementary Material: Supplementary material (schematic diagram of one-pot and continuous spray pyrolysis process, FE-SEM image of the Si nanopowder, TG curve of the MoS_2–C composite microspheres, morphologies of the MoS_2–C composite microspheres without Si nanopowder, XPS Si2p spectra, Nyquist plots, and TEM images after 100 cycles of the MoS_2–C composite microspheres embedded with 30 wt.% Si nanopowder) is available in the online version of this article at http://dx.doi.org/10.1007/s12274-015-0757-3.

References

[1] Armand, M.; Tarascon, J. M. Building better batteries. *Nature* **2008**, *451*, 652–657.

[2] Cheng, F. Y.; Liang, J.; Tao, Z. L.; Chen, J. Functional materials for rechargeable batteries. *Adv. Mater.* **2011**, *23*, 1695–1715.

[3] Cho, J. Porous Si anode materials for lithium rechargeable batteries. *J. Mater. Chem.* **2010**, *20*, 4009–4014.

[4] Szczech, J. R.; Jin, S. Nanostructured silicon for high capacity lithium battery anodes. *Energy Environ. Sci.* **2011**, *4*, 56–72.

[5] Magasinki, A.; Dixon, P.; Hertzberg, B.; Kvit, A.; Ayala, J.; Yushin, G. High-performance lithium-ion anodes using a hierarchical bottom-up approach. *Nat. Mater.* **2010**, *9*, 353–358.

[6] McDowell, M. T.; Lee, S. W.; Nix, W. D.; Cui, Y. 25th anniversary article: Understanding the lithiation of silicon and other alloying anodes for lithium-ion batteries. *Adv. Mater.* **2013**, *25*, 4966–4984.

[7] Choi, N. S.; Chen, Z. h.; Freunberger, S. A.; Ji, X. l.; Sun, Y. K.; Amine, K.; Yushin, G.; Nazar, L. F.; Cho, J.; Bruce, P. G. Challenges facing lithium batteries and electrical double-layer capacitors. *Angew. Chem. Int. Ed.* **2012**, *51*, 9994–10024.

[8] Wu, H.; Cui, Y. Designing nanostructured Si anodes for high energy lithium ion batteries. *Nano Today* **2012**, *7*, 414–429.

[9] Li, X. L.; Zhi, L. J. Managing voids of Si anodes in lithium ion batteries. *Nanoscale* **2013**, *5*, 8864–8873.

[10] Su, X.; Wu, Q. L.; Li, J. C.; Xiao, X. C.; Lott, A.; Lu, W. Q.; Sheldon, B. W.; Wu, J. Silicon-based nanomaterials for lithium-ion batteries: A review. *Adv. Energy Mater.* **2014**, *4*, 1300882.

[11] Liu, X. H.; Zhong, L.; Huang, S.; Mao, S. X.; Zhu, T.; Huang, J. Y. Size-dependent fracture of silicon nanoparticles during lithiation. *ACS Nano* **2012**, *6*, 1522–1531.

[12] Huang, X. K.; Yang, J.; Mao, S.; Chang, J. B.; Hallac, P. B.; Fell, C. R.; Metz, B.; Jiang, J. W.; Hurley, P. T.; Chen, J. H. Controllable synthesis of hollow Si anode for long-cycle-life lithium-ion batteries. *Adv. Mater.* **2014**, *26*, 4326–4332.

[13] Liang, J. W.; Li, X. N.; Zhu, Y. C.; Guo, C.; Qian, Y. T. Hydrothermal synthesis of nano-silicon from silica sol and its lithium ion batteries property. *Nano Res.* **2015**, *8*, 1497–1504.

[14] Li, X. L.; Meduri, P.; Chen, X. L.; Qi, W.; Engelhard, M. H.; Xu, W.; Ding, F.; Xiao, J.; Wang, W.; Wang, C. M. et al. Hollow core–shell structured porous Si–C nanocomposites for Li-ion battery anodes. *J. Mater. Chem.* **2012**, *22*, 11014–11017.

[15] Liu, N.; Lu, Z. D.; Zhao, J.; McDowell, M. T.; Lee, H. W.; Zhao, W. T.; Cui, Y. A pomegranate-inspired nanoscale design for large-volume-change lithium battery anodes. *Nat. Nanotechnol.* **2014**, *9*, 187–192.

[16] Park, Y.; Choi, N. S.; Park, S.; Woo, S. H.; Sim, S.; Jang, B. Y.; Oh, S. M.; Park, S.; Cho, J.; Lee, K. T. Si-encapsulating hollow carbon electrodes via electroless etching for lithium-ion batteries. *Adv. Energy Mater.* **2013**, *3*, 206–212.

[17] Karki, K.; Zhu, Y. J.; Liu, Y.H.; Sun, C. F.; Hu, L. B.; Wang, Y. H.; Wang, C. S.; Cumings, J. Hoop-strong nanotubes for battery electrodes. *ACS Nano* **2013**, *7*, 8295–8302.

[18] Park, M. H.; Kim, M. G.; Joo, J.; Kim, K.; Kim, J.; Ahn, S.; Cui, Y.; Cho, J. Silicon nanotube battery anodes. *Nano Lett.* **2009**, *9*, 3844–3847.

[19] Ge, M. Y.; Rong, J. P.; Fang, X.; Zhou, C. W. Porous doped silicon nanowires for lithium ion battery anode with long cycle life. *Nano Lett.* **2012**, *12*, 2318–2323.

[20] Ge, M. Y.; Rong, J. P.; Fang, X.; Zhang, A. Y.; Lu, Y. H.; Zhou, C. W. Scalable preparation of porous silicon nanoparticles and their application for lithium-ion battery anodes. *Nano Res.* **2013**, *6*, 174–181.

[21] Yoo, J. K.; Kim, J.; Jung, Y. S.; Kang, K. Scalable fabrication of silicon nanotubes and their application to energy storage. *Adv. Mater.* **2012**, *24*, 5452–5456.

[22] Kasavajjula, U.; Wang, C. S.; Appleby, A. J. Nano- and bulk-silicon-based insertion anodes for lithium-ion secondary cells. *J. Power Sources* **2007**, *163*, 1003–1039.

[23] Lai, J.; Guo, H. J.; Wang, Z. X.; Li, X. H.; Zhang, X. P.; Wu, F. X.; Yue, P. Preparation and characterization of flake graphite/silicon/carbon spherical composite as anode materials for lithium-ion batteries. *J. Alloys Compd.* **2012**, *530*, 30–35.

[24] Holzapfel, M.; Buqa, H.; Scheifele, W.; Novák, P.; Petrat, F. M. A new type of nano-sized silicon/carbon composite electrode for reversible lithium insertion. *Chem. Commun.* **2005**, 1566–1568.

[25] Wen, Z. S.; Yang, J.; Wang, B. F.; Wang, K.; Liu, Y. High capacity silicon/carbon composite anode materials for lithium ion batteries. *Electrochem. Commun.* **2003**, *5*, 165–168.

[26] Su, L. W.; Zhou, Z.; Ren, M. M. Core double-shell Si@SiO_2@C nanocomposites as anode materials for Li-ion batteries. *Chem. Commun.* **2010**, *46*, 2590–2592.

[27] Xu, Y. H.; Zhu, Y. J.; Wang, C. S. Mesoporous carbon/silicon composite anodes with enhanced performance for lithium-ion batteries. *J. Mater. Chem. A* **2014**, *2*, 9751–9757.

[28] Jung, D. S.; Hwang, T. H.; Park, S. B.; Choi, J. W. Spray drying method for large-scale and high-performance silicon negative electrodes in Li-ion batteries. *Nano Lett.* **2013**, *13*, 2092–2097.

[29] Fuchsbichler, B.; Stangl, C.; Kren, H.; Uhlig, F.; Koller, S. High capacity graphite–silicon composite anode material for lithium-ion batteries. *J. Power Sources* **2011**, *196*, 2889–2892.

[30] Park, J. B.; Lee, K. H.; Jeon, Y. J.; Lim, S. H.; Lee, S. M. Si/C composite lithium-ion battery anodes synthesized using silicon nanoparticles from porous silicon. *Electrochim. Acta* **2014**, *133*, 73–81.

[31] Wang, B.; Li, X. L.; Zhang, X. F.; Luo, B.; Jin, M. H.; Liang, M. H.; Dayeh, S. A.; Picraux, S. T.; Zhi, L. Adaptable silicon–carbon nanocables sandwiched between reduced graphene oxide sheets as lithium ion battery anodes. *ACS Nano* **2013**, *7*, 1437–1445.

[32] Wang, W.; Ruiz, I.; Ahmed, K.; Bay, H. H.; George, A. S.; Wang, J.; Butler, J.; Ozkan, M.; Ozkan, C. S. Silicon decorated cone shaped carbon nanotube clusters for lithium ion battery anodes. *Small* **2014**, *10*, 3389–3396.

[33] Lin, H. J.; Weng, W.; Ren, J.; Qiu, L. B.; Zhang, Z. T.; Chen, P. N.; Chen, X. L.; Deng, J.; Wang, Y. G.; Peng, H. S. Twisted aligned carbon nanotube/silicon composite fiber anode for flexible wire-shaped lithium-ion battery. *Adv. Mater.* **2014**, *26*, 1217–1222.

[34] Chang, J. B.; Huang, X. K.; Zhou, G. H.; Cui, S. M.; Hallac, P. B.; Jiang, J. W.; Hurley, P. T.; Chen, J. H. Multilayered Si nanoparticle/reduced graphene oxide hybrid as a high-performance lithium-ion battery anode. *Adv. Mater.* **2014**, *26*, 758–764.

[35] Luo, J. Y.; Zhao, X.; Wu, J. S.; Jang, H. D.; Kung, H. H.; Huang, J. X. Crumpled graphene-encapsulated Si nanoparticles for lithium ion battery anodes. *J. Phys. Chem. Lett.* **2012**, *3*, 1824–1829.

[36] Liu, N.; Wu, H.; McDowell, M. T.; Yao, Y.; Wang, C. M.; Cui, Y. A yolk-shell design for stabilized and scalable Li-ion battery alloy anodes. *Nano Lett.* **2012**, *12*, 3315–3321.

[37] Reddy, M. V.; Rao, G. V. S.; Chowdari, B. V. R. Metal oxides and oxysalts as anode materials for Li ion batteries. *Chem.*

Rev. **2013**, *113*, 5364–5457.

[38] Jiang, J.; Li, Y. Y.; Liu, J. P.; Huang, X. T.; Yuan, C. Z.; Lou, X. W. Recent advances in metal oxide-based electrode architecture design for electrochemical energy storage. *Adv. Mater*. **2012**, *24*, 5166–5180.

[39] Cabana, J.; Monconduit, L.; Larcher, D.; Palacín, M. R. Beyond intercalation-based Li-ion batteries: The state of the art and challenges of electrode materials reacting through conversion reactions. *Adv. Mater*. **2010**, *22*, E170–E192.

[40] Armstrong, M. J.; O'Dwyer, C.; Macklin, W. J.; Holmes, J. D. Evaluating the performance of nanostructured materials as lithium-ion battery electrodes. *Nano Res*. **2014**, *7*, 1–62.

[41] An, Q. Y.; Lv, F.; Liu, Q. Q.; Han, C. H.; Zhao, K. N.; Sheng, J. Z.; Wei, Q. L.; Yan, M. Y.; Mai, L. Q. Amorphous vanadium oxide matrixes supporting hierarchical porous Fe_3O_4/graphene nanowires as a high-rate lithium storage anode. *Nano Lett*. **2014**, *14*, 6250–6256.

[42] Wang, H.; Feng, H. B.; Li, J. H. Graphene and graphene-like layered transition metal dichalcogenides in energy conversion and storage. *Small* **2014**, *10*, 2165–2181.

[43] Huang, X.; Tan, C. L.; Yin, Z. Y.; Zhang, H. 25th anniversary article: Hybrid nanostructures based on two-dimensional nanomaterials. *Adv. Mater*. **2014**, *26*, 2185–2204.

[44] Stephenson, T.; Li, Z.; Olsen, B.; Mitlin, D. Lithium ion battery applications of molybdenum disulfide (MoS_2) nanocomposites. *Energy Environ. Sci*. **2014**, *7*, 209–231.

[45] Zhu, C. B.; Mu, X. K.; van Aken, P. A.; Yu, Y.; Maier, J. Single-layered ultrasmall nanoplates of MoS_2 embedded in carbon nanofibers with excellent electrochemical performance for lithium and sodium storage. *Angew. Chem. Int. Ed*. **2014**, *53*, 2152–2156.

[46] Hwang, H.; Kim, H.; Cho, J. MoS_2 nanoplates consisting of disordered graphene-like layers for high rate lithium battery anode materials. *Nano Lett*. **2011**, *11*, 4826–4830.

[47] Wang, Z.; Chen, T.; Chen, W. X.; Chang, K.; Ma, L.; Huang, G. C.; Chen, D. Y.; Lee, J. Y. CTAB-assisted synthesis of single-layer MoS_2–graphene composites as anode materials of Li-ion batteries. *J. Mater. Chem. A* **2013**, *1*, 2202–2210.

[48] Zhang, Q.; Ge, J. P.; Goebl, J.; Hu, Y. X.; Lu, Z. D.; Yin, Y. D. Rattle-type silica colloidal particles prepared by a surface-protected etching process. *Nano Res*. **2009**, *2*, 583–591.

[49] Zhang, C. F.; Peng, X.; Guo, Z. P.; Cai, C. B.; Chen, Z. X.; Wexler, D.; Li, S.; Liu, H. K. Carbon-coated SnO_2/graphene nanosheets as highly reversible anode materials for lithium ion batteries. *Carbon* **2012,** *50*, 1897–1903.

[50] Liu, K. K.; Zhang, W. J.; Lee, Y. H.; Lin, Y. C.; Chang, M. T.; Su, C. Y.; Chang, C. S.; Li, H.; Shi, Y. M.; Zhang, H. et al. Growth of large-area and highly crystalline MoS_2 thin layers on insulating substrates. *Nano Lett*. **2012**, *12*, 1538–1544.

[51] Wang, Q.; Li, J. H. Facilitated lithium storage in MoS_2 overlayers supported on coaxial carbon nanotubes. *J. Phys. Chem. C* **2007**, *111*, 1675–1682.

[52] Ko, Y. N.; Kang, Y. C.; Park, S. B. Superior electrochemical properties of MoS_2 powders with a MoS_2@void@MoS_2 configuration. *Nanoscale* **2014**, *6*, 4508–4512.

[53] Chang, K.; Geng, D. S.; Li, X. F.; Yang, J. L.; Tang, Y. J.; Cai, M.; Li, R. Y.; Sun, X. L. Ultrathin MoS_2/nitrogen-doped graphene nanosheets with highly reversible lithium storage. *Adv. Energy Mater*. **2013**, *3*, 839–844.

[54] Huang, G. C.; Chen, T.; Chen, W. X.; Wang, Z.; Chang, K.; Ma, L.; Huang, F. H.; Chen, D. Y.; Lee, J. Y. Graphene-like MoS_2/graphene composites: Cationic surfactant-assisted hydrothermal synthesis and electrochemical reversible storage of lithium. *Small* **2013**, 9, 3693–3703.

[55] Liu, H.; Su, D. W.; Zhou, R. F.; Sun, B.; Wang, G. X.; Qiao, S. Z. Highly ordered mesoporous MoS_2 with expanded spacing of the (002) crystal plane for ultrafast lithium ion storage. *Adv. Energy Mater*. **2012**, *2*, 970–975.

[56] Gong, Y. J.; Yang, S. B.; Liu, Z.; Ma, L. L.; Vajtai, R.; Ajayan, P. M. Graphene-network-backboned architectures for high-performance lithium storage. *Adv. Mater*. **2013**, *25*, 3979–3984.

[57] Liu, N. A.; Huo, K. F.; McDowell, M. T.; Zhao, J.; Cui, Y. Rice husks as a sustainable source of nanostructured silicon for high performance Li-ion battery anodes. *Sci. Rep*. **2013**, *3*, 1919.

[58] Choi, S. H.; Kang, Y. C. Yolk–shell, hollow, and single-crystalline $ZnCo_2O_4$ powders: Preparation using a simple one-pot process and application in lithium-ion batteries. *ChemSusChem* **2013**, *6*, 2111–2116.

[59] Ko, Y. N.; Park, S. B.; Kang, Y. C. Design and fabrication of new nanostructured SnO_2-carbon composite microspheres for fast and stable lithium storage performance. *Small* **2014**, *10*, 3240–3245.